Spectroscopic signature of surface states and bunching of bulk subbands in topological insulator (Bi0.4 Sb0.6)2 Te3 thin films

Mulder, L.; Castenmiller, C.; Witmans, F.J.; Smit, S.; Golden, M.S.; Zandvliet, H.J.W.; De Boeij, P.L.; Brinkman, A.

Link to publication

Spectroscopic signature of surface states and bunching of bulk subbands in topological insulator $(Bi_{0.4}Sb_{0.6})_2Te_3$ thin films

Liesbeth Mulder [1,*] Carolien Castenmiller [1,*] Femke J. Witmans [1] Steef Smit [2] Mark S. Golden [2]
Harold J. W. Zandvliet [1] Paul L. de Boeij [1] and Alexander Brinkman [1]

[1] *MESA+ Institute for Nanotechnology, University of Twente, 7500 AE Enschede, The Netherlands*
[2] *Van der Waals-Zeeman Institute, Institute of Physics, University of Amsterdam, 1098 XH Amsterdam, The Netherlands*

High-quality thin films of the topological insulator $(Bi_{0.4}Sb_{0.6})_2Te_3$ have been deposited on $SrTiO_3$ (111) by molecular beam epitaxy. Their electronic structure was investigated by *in situ* angle-resolved photoemission spectroscopy and *in situ* scanning tunneling spectroscopy. The experimental results reveal striking similarities with relativistic *ab initio* tight-binding calculations. We find that ultrathin slabs of the three-dimensional topological insulator $(Bi_{0.4}Sb_{0.6})_2Te_3$ display topological surface states, surface states with large weight on the outermost Te atomic layer, and dispersive bulk energy levels that are quantized. We observe that the bandwidth of the bulk levels is strongly reduced. These bunched bulk states as well as the surface states give rise to strong peaks in the local density of states.

I. INTRODUCTION

Chalcogenide three-dimensional (3D) topological insulators (TIs), such as Bi_2Se_3, Bi_2Te_3 and Sb_2Te_3, are well-known for their topological surface states (TSSs) [1–3]. These metallic surface states, which are characterized by a linear dispersion as well as spin-momentum locking, appear as a Dirac cone at the Γ point. Since Bi_2Te_3 single crystals are intrinsically *n*-doped, and Sb_2Te_3 *p*-doped, alloys of the two have been developed to engineer a material in which the chemical potential is located within, or close to, the bulk band gap [4]. An advantage of a higher Sb/Bi ratio is the shift of the Dirac point (DP) to higher energies, reaching above the top of the bulk valence band (VB) [5].

Due to the spatial extent of the surface state in the z direction, it has been predicted that ultrathin slabs of 3D TIs provide a route to a hybridization gap around the DP [6,7], thereby gapping out the TSSs and paving the way to topologically protected one-dimensional (1D) edge-state transport, very comparable to the quantum spin Hall (QSH) effect in HgTe quantum wells [8–10]. Even though Bi_2Se_3 presents the largest bulk band gap, Bi_2Te_3 and Sb_2Te_3 are predicted to be more appealing candidates to exhibit 1D transport due to their relatively short edge-state decay length in the ultrathin film limit [7,11,12]. While stoichiometric slabs have been well-investigated spectroscopically [13–15], even in the limit of hybridized surface states [16], the electronic structure of ultrathin films of off-stoichiometric $(Bi_{1-x}Sb_x)_2Te_3$ is still relatively unexplored. Zhang *et al.* [5] studied the influence of the stoichiometry on the electronic properties of ultrathin $(Bi_{1-x}Sb_x)_2Te_3$ by means of angle-resolved photoemission spectroscopy (ARPES) and

transport measurements. They show that band structure can be engineered by changing the stoichiometry. Furthermore, quasiparticle interference patterns have been imaged with a scanning tunneling microscope, revealing the dispersion above the Fermi energy (E_F) [17,18].

Here, we investigate the electronic structure of few-nm $(Bi_{0.4}Sb_{0.6})_2Te_3$ by directly comparing the results of multiple techniques. We performed ARPES measurements, scanning tunneling spectroscopy (STS) measurements and *ab initio* tight-binding (TB) calculations. The good agreement between the measured and calculated electronic structure reveals a bunching effect of the bulk sublevels, the identification of Bi/Sb TSSs, as well as Te surface states close to the top of the VB, leading to strong peaks in the density of states (DOS). The modeling shows that for $(Bi_{1-x}Sb_x)_2Te_3$ with $x = 0.6$, the reduced bandwidth is likely caused by a Sb/Bi substitution-induced inversion of the band order near the high-symmetry point Γ. This inversion interchanges the bands close to E_F, while the order at the Z point remains unaltered.

II. MATERIALS AND METHODS

A. Molecular beam epitaxy

For this study, 5 and 10 nm $(Bi_{0.4}Sb_{0.6})_2Te_3$ films were deposited using molecular beam epitaxy (MBE) on gate-tunable, Ti-terminated $SrTiO_3$ (111) substrates in a deposition chamber with a base pressure of about 5.0×10^{-11} mbar. Details on the substrate treatment [19] can be found in the Supplemental Material (SM) [20]. High-purity Bi (6N), Sb (6N), and Te (6N) were evaporated from standard Knudsen effusion cells. During the deposition, the substrate was held at a temperature of 225 °C. A quartz crystal microbalance was used to calibrate the individual material fluxes. To ensure a high crystalline growth while suppressing the amount of Te vacancies, we employed a flux ratio of (Bi+Sb):Te = 1:10, with a

---

035122-1

deposition rate of 0.07 nm/min. To verify the stoichiometry of the deposited film, *in situ* x-ray photoelectron spectroscopy (XPS) spectra were recorded using an Omicron nanotechnology surface analysis system, equipped with a monochromatic aluminium source (Kα x-ray source XM1000).

B. Angle-resolved photoemission spectroscopy

ARPES data were acquired at the Van der Waals-Zeeman Institute. The ARPES spectra are taken at a base temperature of 15 K, using an L1 He-Lamp, emitting linearly, *p*-polarized photons with an energy of 21.2 eV, and an A-1 hemispherical analyzer, both from MB Scientific. The system is equipped with a TMM 304 UV monochromator from Specs. The energy resolution was 15 meV and the angular resolution better than 0.1°. Laser-ARPES spectra were obtained using a fourth harmonic source from APE GmbH, producing 200 nm photons with a corresponding energy of 6.2 eV, with an energy resolution of 5 meV and a k-resolution of 0.002 Å^{-1}. The measurements were performed while maintaining a pressure of $<5.0 \times 10^{-11}$ mbar.

C. Scanning tunneling spectroscopy

Scanning tunneling microscopy (STM) and spectroscopy measurements were performed at 77 K with a low-temperature Omicron ultrahigh vacuum (UHV) STM. The base pressure of the STM chamber was below 1.0×10^{-11} mbar and PtIr tips were used. The *I(V)* spectroscopy experiments were conducted in the constant height mode, i.e., the tunnel current was measured while the sample bias was ramped with the feedback loop disabled. The (normalized) *dI(V)/dV* curves are the numerical derivatives of the *I(V)* recordings. The *dI(V)/dV* and *(dI(V)/dV)/(I(V)/V)* curves were obtained by averaging over many *I(V)* traces recorded at different locations.

D. *Ab initio* tight-binding modeling

The electronic structure of the ternary tetradymite alloy was obtained using a TB approach based on the *ab initio* Green's function calculations of Aguilera *et al.* [21]. Their projected TB parameters turn out to be very similar for pristine Bi$_2$Te$_3$ and Sb$_2$Te$_3$ [22], resulting in very comparable band dispersions, apart from band inversions along the line $\Gamma - Z$. This close resemblance allows us to interpolate to the alloy system in the following way: the quasiparticle states for the alloy are expanded as wave packets of Bloch-like sums of localized functions:

$$\psi(\mathbf{r}) = \sum_{m\mathbf{k}} c_{m\mathbf{k}} \phi_{m\mathbf{k}}(\mathbf{r}), \qquad (1)$$

$$\phi_{m\mathbf{k}}(\mathbf{r}) = \frac{1}{\sqrt{N}} \sum_{\mathbf{R}} e^{i\mathbf{k}\cdot\mathbf{R}} w_m(\mathbf{r} - \mathbf{R}). \qquad (2)$$

The $w_m(\mathbf{r})$ centered on a Bi or Sb atom are derived, respectively, from the projected Wannier functions of the pristine Bi$_2$Te$_3$ or Sb$_2$Te$_3$ crystals, and when on a Te atom, from either one. The alloy disorder is thus incorporated into this mixed basis, which can reasonably be assumed to inherit the orthogonality of the pristine Wannier functions. The alloy

Hamiltonian elements on the **k** diagonal then reduce to the weighted average of the pristine ones. As these are by far the largest terms, they effectively define a virtual crystal (VC) Hamiltonian for the alloy. The alloy disorder further enters via smaller off-**k**-diagonal elements that may be accounted for in a perturbative expansion. These off-diagonal terms will cause the wave packets to spread over a range of **k** vectors centered around the VC one. As it turns out, it suffices to compute the VC band structure, $\{\epsilon_{n\mathbf{k}}, \psi_{n\mathbf{k}}\}$, to identify the main features in the ARPES measurements. Similarly, we compute the laterally averaged local density of states (LDOS) from the VC dispersions and use the Tersoff-Hamann model [23] to simulate the marginal tunnel currents:

$$\frac{dI}{dV} \propto \sum_{n\mathbf{k}} \delta(\epsilon_{n\mathbf{k}} - \mathrm{e}V) e^{-2\kappa_{n\mathbf{k}}z} |\langle \psi_{n\mathbf{k}} \mid \mathrm{Te}\rangle|^2. \qquad (3)$$

Here the quasiparticle amplitudes at the outermost Te atoms are used to generate the LDOS at the tip position z (9 Å), while accounting for the **k**- and $\epsilon_{n\mathbf{k}}$-dependent inverse decay length $\kappa_{n\mathbf{k}}$, satisfying

$$\kappa_{n\mathbf{k}} = \sqrt{\frac{2m}{\hbar^2}\left(\Phi - \frac{1}{2}\epsilon_{n\mathbf{k}}\right) + k_{\parallel}^2}, \qquad (4)$$

in which Φ (5.4 eV) is the work function. This simulated signal can be decomposed into layer contributions, as in Fig. 4(b), by adding a projective weight $\nu_{n\mathbf{k}} = |\langle\psi_{n\mathbf{k}} \mid \mathrm{A}\rangle|^2$ to the summand for atomic layer A. The same projective weight is used to identify and color code the surface states in the band dispersion in Figs. 2, 3(b), 4(a), and S1.

E. Vacuum transfer

To avoid surface contamination and oxidation, we have transferred the thin films from the MBE system to the XPS, STM, and ARPES systems using a UHV suitcase. The vacuum suitcase is equipped with a nonevaporable getter pump and an ion pump, which together ensured the pressure remained below 1.5×10^{-10} mbar during the transfer process. In the ARPES system, the film has briefly been exposed to a pressure of 3.0×10^{-10} mbar during the transfer of the sample from the suitcase to the main chamber. For a film to arrive at the STM main chamber, the sample has to move through a load lock and preparation chamber with a base pressure of 5.0×10^{-9} mbar and 1.0×10^{-10} mbar, respectively.

III. RESULTS AND DISCUSSION

(Bi$_{1-x}$Sb$_x$)$_2$Te$_3$ crystallizes in the rhombohedral tetradymite crystal structure, as depicted in Fig. 1(a). The (Bi$_{1-x}$Sb$_x$)$_2$Te$_3$ surface-matched unit cell is composed of three quintuple layers (QLs), each of which are approximately 1 nm high and separated from each other by a Van der Waals gap. The QLs consist of five atomic layers in a Te-*X*-Te-*X*-Te stacking, where *X* can either be Bi or Sb. The STM constant current image in Fig. 1(b) reveals the film's surface morphology. The film exhibits triangular islands, reflecting the threefold symmetry of the crystal structure, with single QL terrace step edges, visible in the line profile shown in Fig. 1(c). The 0.2 nm height differences observed in the
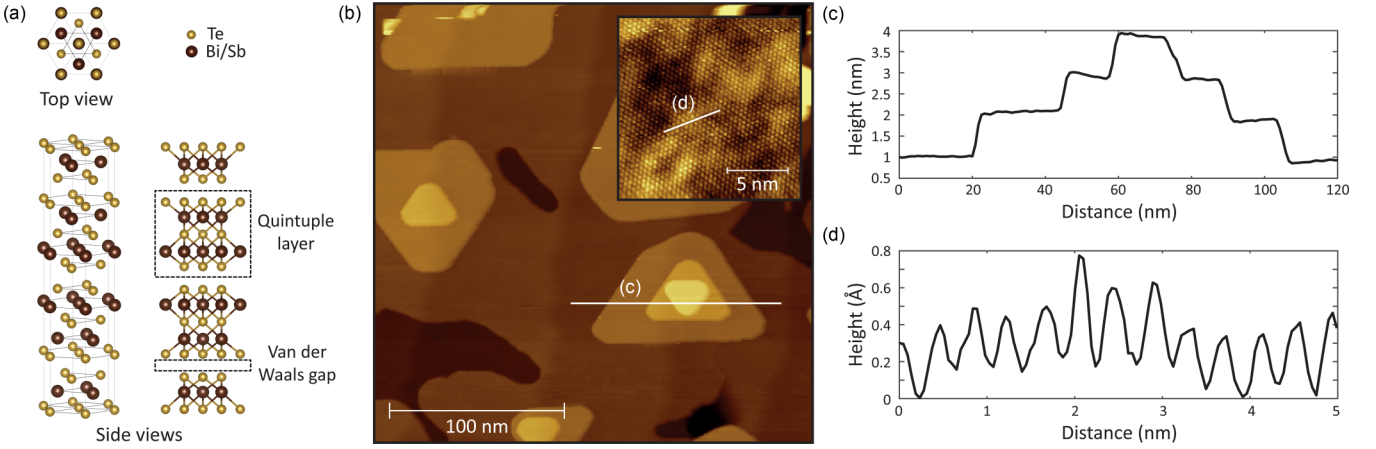
FIG. 1. (a) The layered rhombohedral tetradymite crystal structure of $(Bi_{1-x}Sb_x)_2Te_3$ revealing the quintuple layer stacking along the c axis, which are weakly bonded via Van der Waals interaction. (b) STM topography image (250 x 250 nm) of a 5 nm $(Bi_{0.4}Sb_{0.6})_2Te_3$ film measured at a bias voltage of 1.0 V and a current set point of 400 pA. The inset shows a STM topography image (15 x 15 nm) with the atomic structure on a single terrace measured at a bias voltage of 0.2 V and a current set point of 1.0 nA. The hexagonal structure as shown in (a) is clearly visible. (c) Line profile taken at the white line of the main figure of (b) which crosses a stack of triangular terraces. The height difference at every step edge is approximately 1 nm. The middle terrace is slightly tilted since it is located at a 0.2-nm-high substrate terrace step edge. (d) Line profile taken at the white line of the inset of (b).

background arise from individual Ti-terminated $SrTiO_3$ (111) terrace step edges. The inset of Fig. 1(b) shows a constant current STM image with atomic resolution. The hexagonal atomic arrangement matches the materials crystal structure. Additionally, the extracted line profile, presented in Fig. 1(d), reveals an interatomic distance which is in good agreement with those reported for Bi_2Te_3 and Sb_2Te_3, which exhibit a lattice parameter of approximately 4.39 Å [24] and 4.26 Å [25], respectively. The observed global height inhomogeneity is allocated to disorder-induced charge-density fluctuations [17,18,26].

A. *Ab initio* **tight-binding modeling**

The electronic structure of the $(Bi_{1-x}Sb_x)_2Te_3$ alloys was obtained within the VC approximation of the *ab initio* TB model as outlined above. All slab calculations were performed on free-standing vacuum-surrounded slabs. For the modeling, we take into account all six p-type spin orbitals of every atom in the unit cell, which contains only a single QL for the 3D bulk systems. The covalent bonding inside the QL gives rise to 15 doubly degenerate VBs, of which nine are occupied and six unoccupied, separated by a small gap along the line $F - Z$. We refer to Zhang *et al.* for a schematic of both the bulk and surface Brillouin zones, showing labels for the high-symmetry points [27]. The dispersion along line $\Gamma - Z$, i.e., in the direction perpendicular to the QLs, is small due to the van der Waals bonding type in between the QLs. In the pristine Bi_2Te_3 bulk crystal, we find that the top VB has an energy at Γ that is well below its energy at the Z point. In pristine Sb_2Te_3, the reverse order is obtained. Upon sufficient alloying, we find that in our VC calculations the band order along $\Gamma - Z$ can be tuned, causing the band dispersion along this line to nearly vanish at intermediate alloy fractions close
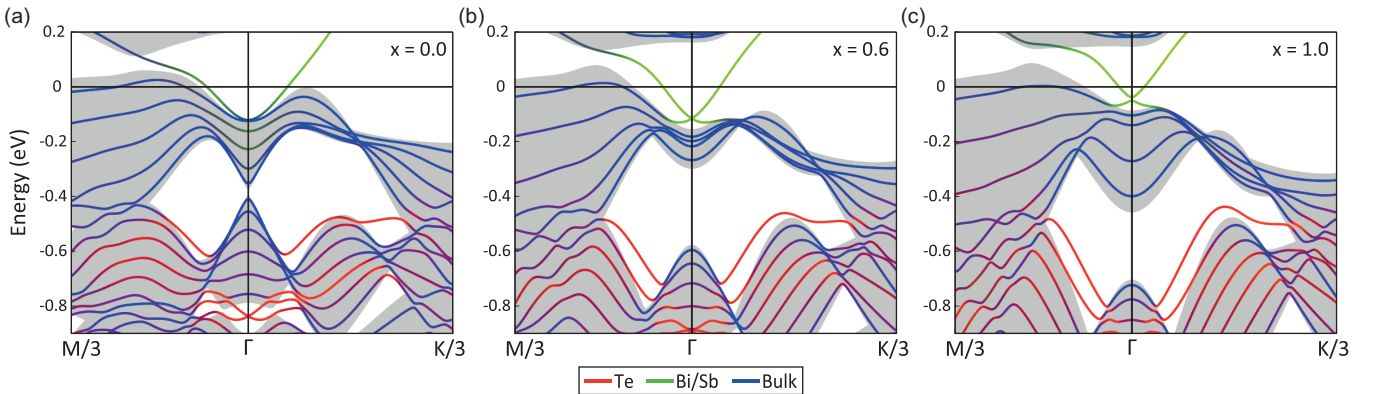
FIG. 2. *Ab initio* TB calculations for a six-QL free-standing thin slab of $(Bi_{1-x}Sb_x)_2Te_3$ in the $M - \Gamma - K$ direction for (a) $x = 0.0$, (b) $x = 0.6$ and (c) $x = 1.0$. The energy is plotted with respect to the predicted E_F. The green, red, and blue lines, respectively, represent Bi/Sb surface states, Te surface states, and states with a bulk character. The grey area marks the projected bulk bands. All states outside this projection represent surface states. The calculations visualize the characteristic shift of the DP with respect to the top of the VB. Furthermore, they show that for mixed stoichiometries, especially close to $x = 0.6$, the bulk states bunch at an energy close to -0.2 eV.
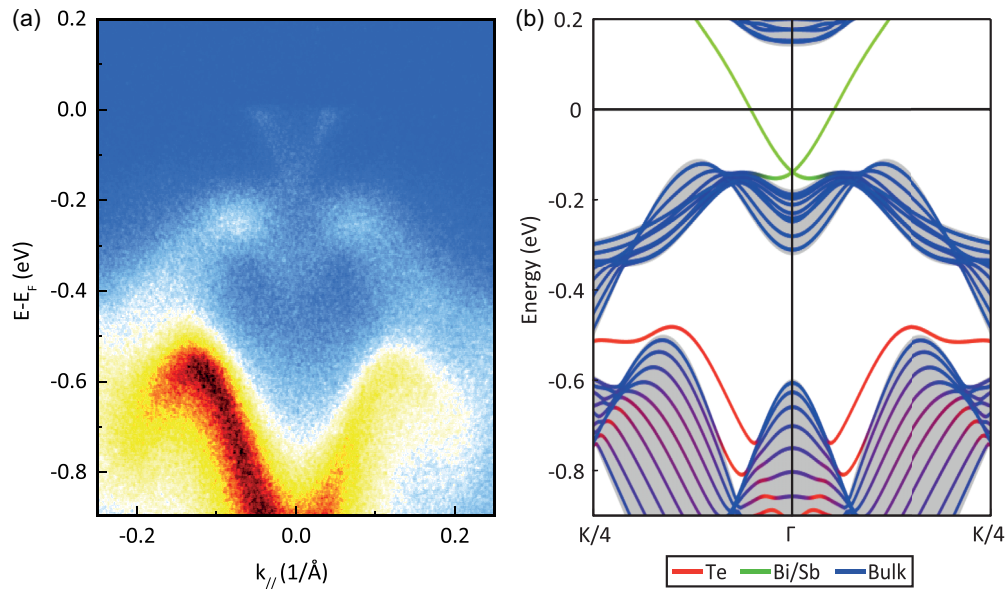
FIG. 3. Correlation between TB calculations and ARPES measurements. (a) ARPES EDM of the band dispersion along the $\bar{K} - \bar{\Gamma} - \bar{K}$ direction of a 10 nm $(Bi_{0.4}Sb_{0.6})_2Te_3$ film deposited on a SrTiO$_3$ (111) substrate. The V-shaped dispersion, at energies above -200 meV, originates from the TSS. The relatively weak M-shaped dispersion just below it, at -200 meV $< E - E_F < -400$ meV, is from the bulk VB. At energies below -500 meV, the Te surface state shows up, which is flanked by bulklike intensity at lower energies. The DP is located in the vicinity of the top of the bulk VB. (b) *Ab initio* TB calculations for a free-standing thin slab, ten QL of $(Bi_{0.4}Sb_{0.6})_2Te_3$, in the $K - \Gamma - K$ direction. The y axis presents the energy of the electronic states with respect to the predicted E_F, resulting from the TB calculations. To allow for a proper comparison between the experimentally observed and theoretically predicted band structure, the TB slab calculation is plotted up until a crystal momentum of K/4 which corresponds to the measured range of 0.25 Å^{-1} in the ARPES EDM.

to 0.6. This has an important effect on the electronic structure of the 2D slabs containing small numbers of QLs. In such systems, the small thickness causes the k vector to quantize along $\Gamma - Z$, and the 2D-projected bulk bands to discretize proportional to the number of QLs, with an energy separation that depends on the alloy fraction x. A flat bulk dispersion along $\Gamma - Z$, causes the bulklike bands to bunch, as shown in

Fig. 2, with a striking reduction of the bandwidth around the Γ point visible in Fig. 2(b).

In addition, TSSs develop from the bulk bands, which separate from these bulklike bands into the gaps that open near Γ. These surface states are only weakly sensitive to the number of QLs. As these surface states live on either side of the slab and decay exponentially into the bulk, the development of
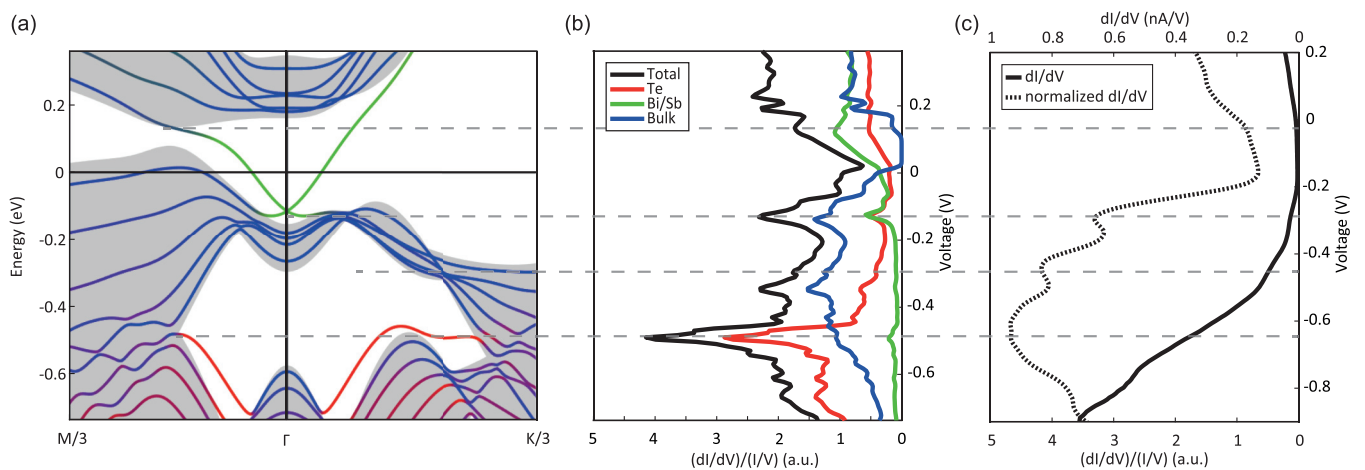
FIG. 4. $(dI/dV)(I/V)$ spectra of a $(Bi_{0.4}Sb_{0.6})_2Te_3$ film as a function of applied bias voltage. (b) STS spectrum based on TB calculations of a six-QL thin slab (a), presenting the contribution of the individual atoms, the bulk, and total contribution to the STS. (c) dI/dV and corresponding DOS of a 5 nm $(Bi_{0.4}Sb_{0.6})_2Te_3$ film on SrTiO$_3$ as a function of applied bias voltage. To allow for a direct comparison between the theoretical predictions by TB calculations (a), (b) and experimental STS data, the energy/bias voltage window of the TB results has been adapted to match the STS spectrum. The oscillations observed in the DOS coincide with both bunched bulk states, near -0.30 V and -0.43 V, as well as the Te contribution to the surface states, near -0.63 V.

the bonding-antibonding gap at Γ is indicative for the decay length. We estimate the decay length to be about three QLs, with an odd-even difference due to the nodal plane inside or in between the middle QLs.

The electronic structure of the slabs, as depicted in Figs. 2, 3(b), 4(a), and S1 are indeed mainly composed of closely spaced parallel bands inside each projected 3D-bulk band (grey) with predominantly bulk character (blue) and a fixed number of surface states that lie outside the projected bulk bands. These surface states are colored green if they have a large weight on the outermost Bi/Sb atoms and red if on the outermost Te layer. The Bi/Sb surface state develops a Dirac cone at Γ for increasing slab thicknesses, as shown in Fig. S1, and is termed TSS. The reversal of the band order at Γ causes the DP to shift from buried inside the VB for Bi_2Te_3 to slightly above the VB for Sb_2Te_3, see Fig. 2.

In the VC approximation, the top-VBs have small energy dispersions over a considerable portion of the Brillouin zone. Such nearly flat bands can easily be localized, and will thus be more sensitive to local disorder in the alloy. This disorder needs to be included in the perturbation expansion going beyond the VC approximation. Furthermore, the additional degeneracy caused by the bunching of these flat, bulklike bands brings about localization not just in the lateral direction but also in the perpendicular direction. This makes them even more susceptible to the alloy disorder. The vicinity of these bands to the DP may cause hybridization of these bands with the TSS, potentially interfering with the delocalized nature of the TSS.

Angle-resolved photoemission spectroscopy

To study the electronic band structure, ARPES measurements have been performed on a nominal 10 nm $(Bi_{0.4}Sb_{0.6})_2Te_3$ film. The resulting electron distribution map (EDM) measured along the $\bar{K} - \bar{\Gamma} - \bar{K}$ direction is presented in Fig. 3(a). On the same film, laser-ARPES measurements were conducted. These results confirm the linearly dispersing TSSs, along with a circular constant energy contour throughout the occupied part of Dirac cone, see Fig. S2. The conformity of the TB model calculations on a vacuum-surrounded slab to the ARPES data from a film of similar thickness, shown in Fig. 3, is striking. The small discrepancy between the E_F in the ARPES EDM and the TB slab calculation can be explained by surface adsorption of residual gases, which is likely to take place when the sample is cooled down to 15 K, at which temperature the ARPES measurements were performed [28]. Additionally, the effect can also be attributed to defects present in the $(Bi_{0.4}Sb_{0.6})_2Te_3$ film. A more in-depth description regarding the observed discrepancy in E_F will follow in the next section. The TSS are relatively weak but clearly resolved in the ARPES EDM at energies above -200 meV, and merge on the lower binding energy side with weak bulklike states between -200 meV and -400 meV. The Te surface state shows up as a much more intense feature in the ARPES below -500 meV, with an expected dispersion and flanked at the lower energy side by bulklike intensity. The difference in intensity between the surface states and the bulk bands in the EDM can be explained by taking into consideration that, for a photon energy of 21.2 eV, the

escape depth of the emitted electron is of the order of only a couple of nm. This means that we expect the surface states with large weight on the outermost Te atomic layer to be more intense than those with large weight on the Bi/Sb layer beneath. Moreover, we also expect these surface states to be more intense than the bulklike states from the layers below, even though the latter are greater in number. In particular, we observe that the Te surface state is asymmetrically sensitive to the p-polarized light, while the bulklike states and the TSS are more symmetric. A more detailed description is provided in the SM.

The location of the DP, E_D, with respect to the top of the VB, along $K - \Gamma - K$, as found in the TB calculations is slightly different than observed in ARPES. From the ARPES EDM, we find the DP to lie approximately 50 meV above the top of the VB, whereas in the TB slab calculation E_D coincides with the top of the bunched VB bulk states in the $\Gamma - K$ direction. By extracting the Dirac fermion velocity from the linear dispersion around the DP from the ARPES EDM, using an undistorted upper cone fitted to the $\bar{\Gamma} - \bar{K}$ dispersion angle, we find v_F to be about 4.7×10^5 m/s. By applying the same procedure on the TB-calculated TSS dispersion, we find a v_F of 4.1×10^5 m/s, which closely resembles the experimental value. Additionally, these values are also in good correspondence with previously published calculations [27] and ARPES data [4]. However, in the TB slab calculations, we note that at energies just below E_D, the TSS present a flat-band behavior, causing them to exhibit a nonlinear behavior at energies close to the VB.

B. Scanning tunneling spectroscopy

The subband spacing in Sb_2Te_3 determined by quantum confinement was previously shown to give rise to weak oscillations in the DOS, as revealed by STS [16]. The quantum well states were shown to vary with the thickness of the slab. We anticipate that the situation is very different for $(Bi_{1-x}Sb_x)_2Te_3$: the bunched nature of the quantum well states should give a strong signal in STS and the peak positions are mainly given by the energies where the bands are flat. In $(Bi_{0.4}Sb_{0.6})_2Te_3$, this bunching effect of flat bands turns out to occur, at comparable $E - E_F$, independent of the slab thickness, see Fig. S1.

STS data can, in some cases, also provide information on the dispersion of the energy bands [29], as elucidated in the SM. We show that the extracted Fermi velocity, v_F, from the voltage dependence of the inverse decay length in the vicinity of the DP gives a v_F of about 1.5×10^5 m/s. Note that this value is significantly lower than the v_F extracted from the ARPES EDM, because the latter v_F was extracted higher up in the cone. This is in excellent agreement with the approximately 2.4×10^5 m/s found using our TB model by considering the apex to be at -0.15 eV relative to E_F, and the tangent at the DP.

We use the Tersoff-Hamann model to simulate the tunnel currents using the LDOS derived from our TB model [23]. This way, we are able to resolve the contribution of the electronic bands to the total dI/dV of an STS spectrum. The band structure for a free-standing six-QL $(Bi_{0.4}Sb_{0.6})_2Te_3$ film is presented in Fig. 4(a). The resulting simulation of

the corresponding STS spectrum is shown in Fig. 4(b). The $k_\parallel$-dependent decay length of the states into the vacuum will cause the STS to be most sensitive to the dispersions close to the Γ point and, in particular, to the ones giving rise to van Hove singularities. This is clearly observed in the computed normalized dI/dV curves in Fig. 4(b). Our TB calculations reveal that the LDOS in the VB is dominated by a Te surface state contribution whose location and character is unchanged on altering the thickness, as can be seen in Fig. S1, and to variation in the alloy fraction.

The STS measurement of a 5-nm-thin $(Bi_{0.4}Sb_{0.6})_2Te_3$ film in Fig. 4(c) shows all the important features that can also be recognized in the TB calculations presented in Figs. 4(a) and 4(b). In the TB calculation, E_F is locked to the top of the bulk VB around M/6. The recorded STS spectrum, however, reveals that, experimentally, E_F tends to shift to the bottom of the conduction band. In the SM, an additional STS measurement is presented, which was performed on another 5-nm-thin $(Bi_{0.4}Sb_{0.6})_2Te_3$ film and shows the same weak oscillations in the DOS with a similar peak separation, but with the E_F at a different position, see Fig. S3. This discrepancy of the location of the E_F observed when comparing the results from Fig. S3 with those presented in the main text is more frequently observed when comparing individual spectroscopy results from sample to sample, and even when comparing different terraces on a single sample. This variation can be attributed to either the adsorption process of molecules to the film surface or the presence of defects in the material, such as Te vacancies. To present an estimate of the shift of the E_F that can be induced in the material by Te vacancies, we first make the assumption that E_F is located within the bulk band gap and only crosses the TSS, characterized by a linear dispersion with $v_F = 4.7 \times 10^5$ m/s. For this dispersion, a shift of 100 meV is accompanied by a wave vector change of about 3.2×10^8 m^{-1}, which corresponds to a 2D carrier density, n_{2D}, of 8.3×10^{11} cm^{-2}. Assuming that every missing Te atom dopes the system with a single electron, this n_{2D} can already be induced when about 0.15% of the unit cells on the film surface exhibit a single Te vacancy. Therefore, we can argue that the shift of about 0.15 eV for the comparison in Fig. 4 is justified.

The $(dI(V)/dV)/(I(V)/V)$ curve, the dashed line in Fig. 4(c), shows three distinct peaks that are closely correlated to DOS oscillations found in the TB STS simulation. Looking at the first peak found in the DOS of the STS measurement, at approximately -0.30 V, the TB STS simulation reveals that the origin of this local maximum in DOS originates from the sum of the DOS arising from both the flat bunching bulk states in the $\Gamma - K$ direction and the flat Bi/Sb surface state band just below the DP. Since these local maxima occur at an energy very close to E_D, it is difficult to point out the exact location of the DP from the signal of the total DOS alone. The second peak in the normalized $dI(V)/dV$ curve located at -0.43 V can also be attributed to arise from bunching bulk states. However, for these states the state bunching occurs closer to the K point along the line $\Gamma - K$, namely, around K/6. The third, broad peak in the normalized $dI(V)/dV$ curve stems from the Van Hove singularity of the upper red surface

state in the TB calculation in Fig. 4(a). These Te surface states are nearly degenerate in energy over a large part of the BZ in the VC. These may combine to form well-localized quasiparticle states in the alloy, which will spread over a range of energies due to the disorder. The predicted Van Hove singularity in the VC may thus become broadened in the true alloy. A similar effect will be expected near the minima of the TSS with large weight on Bi/Sb. As the disorder is more pronounced in this layer as compared to the Te one, we expect a larger broadening effect here as compared to the Te surface state.

Since we found that the location of the subbands is rather invariant upon changing the film thickness, we are also able to state that the STS measurement matches the results from our ARPES study, presented in Fig. 3(a). Therefore, we can state that the combination of our theoretically predicted electronic structure, using a TB approach, and the spectroscopy experiments provides an adequate and complete picture of the electronic properties of our material system.

IV. CONCLUSION

In summary, the TB modeling shows that the bunching of bulk subbands in the alloy $(Bi_{0.4}Sb_{0.6})_2Te_3$ is likely caused by a Sb/Bi substitution induced change in band order, close to E_F near Γ, with the TSS still separated from the VB. The fact that the DP lies in close proximity to the bunched bulk subbands, which are vulnerable to alloy disorder, makes this material system the perfect platform to investigate the robustness of the TSS against disorder. The close correlations between the TB slab calculations and ARPES measurements allow us to elaborate on the atomic origin of electronic bands near E_F, providing a good understanding of the electronic structure of an alloy of the TI $(Bi_{1-x}Sb_x)_2Te_3$. By combining the results acquired in the spectroscopy experiments and TB calculations we are able to attribute the oscillatory behavior of the DOS in the STS measurements, performed on 5 nm $(Bi_{0.4}Sb_{0.6})_2Te_3$ films, to the flat bunching states with a bulk character and to the Van Hove singularity of the Te surface state in the VB.

This detailed understanding of the material system will allow for future experiments in the direction of even thinner slabs where a hybridization gap will be induced in the TSS. Devices can be equipped with a gate to tune into the hybridization gap that occurs at the DP, hereby enabling access to the topological edge states. The spectroscopy measurements confirmed that the DP is in close proximity to the bulk VB. Therefore, to observe signatures of a possible QSH state, for example, via magneto-transport measurements, the stoichiometry still shows some room for further optimization. We present Sb_2Te_3 as another possible candidate to perform future research to the QSH state of matter.

ACKNOWLEDGMENTS

[1] H.-J. Noh, H. Koh, S.-J. Oh, J.-H. Park, H.-D. Kim, J. D. Rameau, T. Valla, T. E. Kidd, P. D. Johnson, Y. Hu, and Q. Li, Spin-orbit interaction effect in the electronic structure of Bi_2Te_3 observed by angle-resolved photoemission spectroscopy, Europhys. Lett. **81**, 57006 (2008).

[2] Y. Xia, D. Qian, D. Hsieh, L. Wray, A. Pal, H. Lin, A. Bansil, D. Grauer, Y. S. Hor, R. J. Cava, and M. Z. Hasan, Observation of a large-gap topological-insulator class with a single Dirac cone on the surface, Nat. Phys. **5**, 398 (2009).

[3] Y. L. Chen, J. G. Analytis, J.-H. Chu, Z. K. Liu, S.-K. Mo, X. L. Qi, H. J. Zhang, D. H. Lu, X. Dai, Z. Fang, S. C. Zhang, I. R. Fisher, Z. Hussain, and Z.-X. Shen, Experimental realization of a three-dimensional topological insulator, Bi_2Te_3, Science **325**, 178 (2009).

[4] X. He, T. Guan, X. Wang, B. Feng, P. Cheng, L. Chen, Y. Li, and K. Wu, Highly tunable electron transport in epitaxial topological insulator $(Bi_{1−x}Sb_x)_2Te_3$ thin films, Appl. Phys. Lett. **101**, 123111 (2012).

[5] J. Zhang, C.-Z. Chang, Z. Zhang, J. Wen, X. Feng, K. Li, M. Liu, K. He, L. Wang, X. Chen, Q.-K. Xue, X. Ma, and Y. Wang, Band structure engineering in $(Bi_{1−x}Sb_x)_2Te_3$ ternary topological insulators, Nat. Commun. **2**, 574 (2011).

[6] J. Linder, T. Yokoyama, and A. Sudbø, Anomalous finite size effects on surface states in the topological insulator Bi_2Se_3, Phys. Rev. B **80**, 205401 (2009).

[7] C.-X. Liu, H. J. Zhang, B. Yan, X.-L. Qi, T. Frauenheim, X. Dai, Z. Fang, and S.-C. Zhang, Oscillatory crossover from two-dimensional to three-dimensional topological insulators, Phys. Rev. B **81**, 041307(R) (2010).

[8] B. A. Bernevig, T. L. Hughes, and S.-C. Zhang, Quantum spin Hall effect and topological phase transition in HgTe quantum wells, Science **314**, 1757 (2006).

[9] M. König, S. Wiedmann, C. Brüne, A. Roth, H. Buhmann, L. W. Molenkamp, X.-L. Qi, and S.-C. Zhang, Quantum spin Hall insulator state in HgTe quantum wells, Science **318**, 766 (2007).

[10] B. Zhou, H. Z. Lu, R. L. Chu, S. Q. Shen, and Q. Niu, Finite Size Effects on Helical Edge States in a Quantum Spin-Hall System, Phys. Rev. Lett. **101**, 246807 (2008).

[11] M. Kim, C. H. Kim, H. S. Kim, and J. Ihm, Topological quantum phase transitions driven by external electric fields in Sb_2Te_3 thin films, Proc. Natl. Acad. Sci. **109**, 671 (2012).

[12] M. M. Asmar, D. E. Sheehy, and I. Vekhter, Topological phases of topological-insulator thin films, Phys. Rev. B **97**, 075419 (2018).

[13] Y. Jiang, Y. Wang, M. Chen, Z. Li, C. Song, K. He, L. Wang, X. Chen, X. Ma, and Q. K. Xue, Landau Quantization and the Thickness Limit of Topological Insulator Thin Films of Sb_2Te_3, Phys. Rev. Lett. **108**, 016401 (2012).

[14] L. Plucinski, A. Herdt, S. Fahrendorf, G. Bihlmayer, G. Mussler, S. Döring, J. Kampmeier, F. Matthes, D. E. Bürgler, D. Grützmacher, S. Blügel, and C. M. Schneider, Electronic structure, surface morphology, and topologically protected surface states of Sb_2Te_3 thin films grown on Si(111), J. Appl. Phys. **113**, 053706 (2013).

[15] P. Ngabonziza, R. Heimbuch, N. de Jong, R. A. Klaassen, M. P. Stehno, M. Snelder, A. Solmaz, S. V. Ramankutty, E. Frantzeskakis, E. van Heumen, G. Koster, M. S. Golden, H. J. W. Zandvliet, and A. Brinkman, In situ spectroscopy of intrinsic Bi_2Te_3 topological insulator thin films and impact of extrinsic defects, Phys. Rev. B **92**, 035405 (2015).

[16] Y. Jiang, Y. Y. Sun, M. Chen, Y. Wang, Z. Li, C. Song, K. He, L. Wang, X. Chen, Q. K. Xue, X. Ma, and S. B. Zhang, Fermi-Level Tuning of Epitaxial Sb_2Te_3 Thin Films on Graphene by Regulating Intrinsic Defects and Substrate Transfer Doping, Phys. Rev. Lett. **108**, 066809 (2012).

[17] X. He, H. Li, L. Chen, and K. Wu, Substitution-induced spin-splitted surface states in topological insulator $(Bi_{1−x}Sb_x)_2Te_3$, Sci. Rep. **5**, 8830 (2015).

[18] K. L. Scipioni, Z. Wang, Y. Maximenko, F. Katmis, C. Steiner, and V. Madhavan, Role of defects in the carrier-tunable topological-insulator $(Bi_{1−x}Sb_x)_2Te_3$ thin films, Phys. Rev. B **97**, 125150 (2018).

[19] G. Koster, B. L. Kropman, G. J. H. M. Rijnders, D. H. A. Blank, and H. Rogalla, Quasi-ideal strontium titanate crystal surfaces through formation of strontium hydroxide, Appl. Phys. Lett. **73**, 2920 (1998).

[20] See Supplemental Material at https://link.aps.org/supplemental/10.1103/PhysRevB.105.035122 for information regarding the substrate treatment, an explanation of the asymmetry observed in the ARPES EDM using the ARPES selection rules, thickness-dependent TB calculations, laser-ARPES spectra, a description of the Dirac velocity determination by STS, and an additional STS measurement.

[21] I. Aguilera, C. Friedrich, and S. Blügel, Many-body corrected tight-binding Hamiltonians for an accurate quasiparticle description of topological insulators of the Bi_2Se_3 family, Phys. Rev. B **100**, 155147 (2019).

[22] Which requires a phase factor $−1$ for the Sb $5p$ states relative to the Bi $6p$ states.

[23] J. Tersoff and D. R. Hamann, Theory of the scanning tunneling microscope, Phys. Rev. B **31**, 805 (1985).

[24] S. Nakajima, The crystal structure of $Bi_2Te_{3−x}Se_x$, J. Phys. Chem. Solids **24**, 479 (1963).

[25] T. L. Anderson and H. B. Krause, Refinement of the Sb_2Te_3 and Sb_2Te_2Se structures and their relationship to nonstoichiometric $Sb_2Te_{3−y}Se_y$ compounds, Acta Crystallographica Section B **30**, 1307 (1974).

[26] B. Jäck, F. Zinser, E. J. König, S. N. P. Wissing, A. B. Schmidt, M. Donath, K. Kern, and C. R. Ast, Visualizing the multifractal wave functions of a disordered two-dimensional electron gas, Phys. Rev. Research **3**, 013022 (2021).

[27] H. Zhang, C.-X. Liu, X.-L. Qi, X. Dai, Z. Fang, and S.-C. Zhang, Topological insulators in Bi_2Se_3, Bi_2Te_3 and Sb_2Te_3 with a single Dirac cone on the surface, Nat. Phys. **5**, 438 (2009).

[28] C. Chen, S. He, H. Weng, W. Zhang, L. Zhao, H. Liu, X. Jia, D. Mou, S. Liu, J. He, Y. Peng, Y. Feng, Z. Xie, G. Liu, X. Dong, J. Zhang, X. Wang, Q. Peng, Z. Wang, S. Zhang, F. Yang, C. Chen, Z. Xu, X. Dai, Z. Fang, and X. J. Zhou, Robustness of topological order and formation of quantum well states in topological insulators exposed to ambient environment, Proc. Natl. Acad. Sci. **109**, 3694 (2012).

[29] Z. Jiao and H. J. W. Zandvliet, Determination of the Fermi velocity of graphene on MoS_2 using dual mode scanning tunneling spectroscopy, Appl. Phys. Lett. **118**, 163103 (2021).